

# The Oxygen Vacancy in Crystal Phases of WO<sub>3</sub>

Ryan Chatten,<sup>\*,†</sup> Alan V. Chadwick,<sup>†</sup> Aline Rougier,<sup>‡</sup> and Philip J. D. Lindan<sup>†</sup>

Physics Laboratory, School of Physical Sciences, University of Kent, Canterbury CT2 7NR, United Kingdom,  
and Laboratoire de Reactivite et Chimie des Solides, Universite de Picardie Jules Verne, 33 rue St. Leu,  
80039 Amiens, Cedex, France

Received: September 24, 2004; In Final Form: November 26, 2004

The oxygen vacancy in WO<sub>3</sub> has previously been implicated in the electrochromism mechanism in this material. Previous theoretical calculations on the oxygen vacancy in WO<sub>3</sub> have not considered the full range of crystal structures adopted by the material. Here we report studies of the oxygen vacancy in seven crystal phases. The use of a very accurate tungsten plane-wave pseudopotential means that a byproduct of this study is a more detailed and complete picture of undefected WO<sub>3</sub> than previously available. Electronic structures of the crystal phases in both undefected and defected systems have been calculated and are discussed. The band gap in WO<sub>3</sub> is dependent upon bonding–antibonding interactions, these being dependent upon overlap in each direction. The effect of an oxygen vacancy is dependent upon the availability of both Op and Wd electrons, this being different for the various phases. A variety of behavior is predicted, which may be explained in terms of O2p–W5d mixing, including the formation of long W–W dimer bonds. It is found that the nature of a polaron in this material is dependent upon both the crystal structure and distribution of oxygen vacancies.

## I. Introduction

The main interest in WO<sub>3</sub> is due to its electrochromic properties. Reduction of either transparent WO<sub>3</sub> single crystals or yellow-green WO<sub>3</sub> powder results in blue coloration,<sup>1</sup> the color centers generally being attributed to electron excess localized on W ions (W<sup>5+</sup>).<sup>2</sup> Oxygen vacancies have been proposed as color centers<sup>3</sup> as this is a simple way of inducing electron excess. Coloration may be induced by a variety of means such as electrochromism, photochromism, and thermochromism though these share the common underlying mechanism<sup>4,5</sup> of changing the charge state of tungsten. Electrochromism refers to the reversible and persistent change in optical properties upon application of an electric potential and is of greatest technological interest.

Experimental evidence for the importance of the oxygen vacancy to electrochromic properties is extensive. It is observed that WO<sub>3–y</sub> films exhibit different chromic properties for different levels of oxygen deficiency:  $y > 0.5$  films are metallic and conductive,  $y = 0.3–0.5$  films are blue and conductive, and  $y < 0.3$  films are transparent and resistive,<sup>6</sup> these findings being independent of the film preparation method. A decrease in band gap from  $\sim 3.2$  eV to  $\sim 2.5$  eV is noted for  $y < 0.3$  films upon raising formation temperature from room temperature to 400 °C, this correlating to a decrease in the ratio of W–O double bonds to single bonds.<sup>7–9</sup> This effect may be attributed to the formation of W<sup>5+</sup> at a surface due to charge balancing.<sup>10</sup> The importance of surface area and interphase boundaries to the W charge state is well-documented.<sup>11–13</sup>

Intervalence charge transfer (IVCT)<sup>14</sup> and small polaron absorption<sup>15</sup> theories are the most widely accepted models to explain chromic properties. The IVCT model considers W<sup>5+</sup> formation from the localization of excess electrons on W<sup>6+</sup> sites.

Absorption of a photon results in the transport of an electron in one W<sup>5+</sup> site to a neighboring W<sup>6+</sup> site. There are, however, several places where the color center may be located: The excess electron can be localized (small polaron), delocalized on a few ions (large polaron), or infinitely delocalized (conduction electron). In the small polaron model, the excess electron and associated lattice distortion may be described as a polaron, this hopping from one site to the next ( $h\nu + \text{W}^{5+}_{(\text{A})} + \text{W}^{6+}_{(\text{B})} \rightarrow \text{W}^{5+}_{(\text{B})} + \text{W}^{6+}_{(\text{A})} + E_{\text{phonon}}$ ).

Both the IVCT and small polaron models are unable to explain the colorless nature of  $y < 0.3$  films or the observation that a decrease in coloring efficiency is related to a decrease in oxygen deficiency.<sup>16</sup> A modification to the small polaron model has been proposed in which the host contains W<sup>4+</sup> and W<sup>6+</sup> states while W<sup>5+</sup>, necessary for coloration, is formed from electron addition to W<sup>6+</sup> ions.<sup>6,17,18</sup> The oxygen vacancy has a pivotal role in generating the lower charge state ions. The W<sup>4+</sup>–W<sup>6+</sup> small polaron model is able to explain the proportionality between coloration efficiency and oxygen deficiency<sup>6</sup> and also explains the lack of W<sup>5+</sup> states at small oxygen deficiencies. The existence of W<sup>5+</sup> and W<sup>4+</sup> species is still a matter of some debate with W<sup>5+</sup> bipolarons also postulated.<sup>19</sup> Readers are referred to the reviews by Granqvist<sup>1,20</sup> for further details of the proposed electrochromic mechanisms.

It is clear that the structure has a major impact on electrochromic properties.<sup>21</sup> WO<sub>3</sub> is composed of corner sharing octahedra of varying distortion. The deviation from the simple cubic structure seen in ReO<sub>3</sub> is due to a second-order Jahn–Teller distortion.<sup>22</sup> Several distortions are possible with phase ordering thought to be monoclinic *Pc* from  $-140$  to  $-50$  °C,<sup>23</sup> triclinic *P1* from  $-50$  to  $17$  °C,<sup>24–28</sup> monoclinic *P21-n* from  $17$  to  $330$  °C,<sup>24,29,30,27</sup> orthorhombic *Pmnb* from  $330$  to  $740$  °C,<sup>31–34</sup> and tetragonal *P4-nmm* above  $740$  °C.<sup>35,31,34</sup> At  $\sim 830$  °C a tetragonal structure of space group *P4-ncc* may be observed.<sup>36</sup> The firm assignment of space groups to the

\* Address correspondence to this author. E-mail: r.chatten@kent.ac.uk.

<sup>†</sup> University of Kent.

<sup>‡</sup> Universite de Picardie Jules Verne.

monoclinic phases is still debated with  $P21-a$ ,<sup>37,38</sup>  $Pc$ ,<sup>25,28,39</sup>  $P21-c$ ,<sup>28</sup>  $P21-n$ ,<sup>24,29,30,27</sup> and other variants proposed.

There have been numerous theoretical studies on WO<sub>3</sub> crystals including recent self-consistent, first principles calculations<sup>40–44</sup> though these studies were generally confined to the simple cubic system. There has been only one previous density functional study examining the multiple phases commonly found.<sup>39</sup> Our findings are compared to the findings of these earlier works in the results section of this paper.

The simple cubic phase is known to contain a 2nd-order Jahn–Teller distortion and is therefore unstable, though previous theoretical work has concentrated on this structure for reasons of computational simplicity and it is included here to allow valuable comparisons between theoretical techniques. It is worth noting that the argument for the simple cubic phase to be considered a good model for the distorted structures has long been disproven.<sup>21</sup> While many claim<sup>45–47</sup> to have synthesized cubic WO<sub>3</sub>, it has recently been demonstrated that these structures were stabilized by the presence of impurities.<sup>48</sup>

The characterization of the oxygen vacancy in each phase is deemed to be of importance since the wide range of formation techniques used to produce electrochromic films and the range of operating conditions expected of an electrochromic device affect the crystal structure and hence electronic properties. Of particular importance are monoclinic, triclinic, and orthorhombic phases as any of these may form in the common film substrate deposition temperature range of room temperature to 400 °C. This work examines the effect of oxygen deficiency for several ( $Pm-3m$ ,  $P21-c$ ,  $P21-m$ ,  $Pmnb$ ,  $P1$ ,  $P4nmm$ ,  $P4ncc$ ) crystalline phases. The main aim of this work is to determine the nature of the polaron in WO<sub>3</sub> systems containing an oxygen defect as this understanding is currently lacking in small polaron models. Characterization of these systems should be seen as a necessary first step in modeling electrochromism since the oxygen vacancy is of such fundamental importance and has received little theoretical attention.

## II. Computational Method

All calculations were performed with the plane-wave pseudopotential density functional theory as implemented in the CASTEP code.<sup>49</sup> Vanderbilt ultrasoft pseudopotentials<sup>50</sup> were used throughout as was the revised Perdew–Becke–Ernzerhof exchange and correlation functional.<sup>51</sup> All calculations employed 3D periodic boundary conditions.

Previous density functional theoretic treatments of WO<sub>3</sub> have been hampered by an overestimation of lattice parameters and an underestimate of band gap. This is generally attributed to self-interaction,<sup>52</sup> which pushes all occupied levels up in energy. Using the results of all-electron calculations, a fully nonlocal pseudopotential incorporating semi-core states (6s and 6p) as valence states has been developed and used throughout this work. Specifically, a nuclear charge of 74, with 14 valence electrons in total, and radii of 2.1 Å were used as input within the freely available Vanderbilt ultrasoft pseudopotential generator.<sup>53</sup> The Koelling–Harmon scalar relativistic wave equation was used in all-electron calculations on the W atom, the calculated wave function being used to optimize a plane-wave pseudopotential by minimization of the scattering within each angular momentum channel. The performance of this pseudopotential is examined critically within the results section of this paper though it is worth noting that tests on tungsten metal and tungsten carbide yielded predictions of lattice constant only 0.19% less than the experimental value in the case of W metal and 0.31% and 0.63% less than the experimental values for WC

$a = b$  and  $c$  lattice constants, respectively. A relatively high cutoff energy of 500 eV was imposed on the plane-wave expansion for both W and O, this being found necessary to achieve good structural convergence.

Trial structures for the various phases were obtained from the literature cited in the previous section. These structures were relaxed until the unit cell was found to change by less than 0.1 Å<sup>3</sup> between subsequent optimizations. Final structures were optimized by using a force tolerance of  $5 \times 10^{-2}$  eV/Å and energies were made self-consistent to an accuracy of  $1 \times 10^{-6}$  eV/atom. Sampling of the reciprocal Brillouin zone was dependent upon the symmetry though the maximum  $k$ -point spacing was 0.05 Å<sup>-1</sup>. Convergence tests on simple cubic WO<sub>3</sub> were performed to arrive at the cutoff energy and Brillouin zone sampling parameters used throughout. To overcome the Fermi discontinuity, where populations flip between 0 and 1 upon subsequent energy minimizations, a smearing width of 0.1 eV was employed though the results presented have been extrapolated to zero temperature by using the method of Gillan.<sup>54</sup> Vacancies are modeled as neutral entities such that the vacancy formation energy is with respect to half the energy of a neutral, triplet spin-state O<sub>2</sub> molecule, relaxed within that particular cell geometry with identical sampling parameters.

In the results that follow band structures have been computed by evaluating the Kohn–Sham eigenvalues at symmetrically important  $k$ -points in the reciprocal Brillouin zone and at  $k$ -points on trajectories between these points. Assignment of these bands to specific bonds has been performed by visualization of charge density isosurfaces and slices on a band-by-band basis.

## III. Results and Discussion

This section is structured as follows: First the structures and energies of undefected phases are presented and compared to previous work in section A. The electronic structure results for undefected phases are presented and discussed for each structure in turn in subsections A.1–5. The findings for the undefected system are then summarized in subsection A.6. The results for the oxygen vacancy are then presented and discussed in a similar fashion in section B. Due to the large amount of data produced in analyzing the electronic structures of each system only representative results are given in order that the effects discussed in the text may be visualized.

**A. Undefected Phases of WO<sub>3</sub>.** Numerous structures have been proposed for the low- and high-temperature phases of monoclinic WO<sub>3</sub>. Relaxation of the atomic positions within an optimized  $P21-n$  unit-cell yielded a structure best described as  $P21-m$ , though strictly this structure is contained within the  $P1$  space group. Similarly optimization of the atomic positions of a  $Pc$  optimized cell yielded  $P21-c$ , this in agreement with earlier work.<sup>39</sup> The results presented here are for optimized cells and atomic positions of the  $P21-m$  and  $P21-c$  systems, these representing the high- and low-temperature monoclinic phases, respectively.

All W–O bond lengths are equal in the simple cubic structure at 1.902 Å, the unit cell occupying a volume of 55.03 Å<sup>3</sup>. The lattice cell volume for each phase is given in Table 1, and the maximum and minimum W–O bond lengths in each direction are given in Table 2. Previous theoretical and experimental determinations of the lattice volume are given in Table 3 for many phases. The implication of impurities in stabilizing the simple cubic structure means that the experimental volumes should be treated with considerable caution. It is notable that the predicted lattice volume is 2.3% smaller than a previous GGA determination<sup>39</sup> and is closer to experimental values.

**TABLE 1: WO<sub>3</sub> Volumes, Energies, and Band Gaps of Several Crystal Phases<sup>a</sup>**

crystal	space group	$E_{\text{WO}_3}/\text{eV}$	$\text{vol}/\text{\AA}^3$	$E_G/\text{eV}$
simple cubic	<i>Pm-3m</i>	-3378.423	55.03	0.69 (R-Γ)
monoclinic	<i>P21-c</i>	-3378.576	56.90	1.71 (Z-Γ)
monoclinic	<i>P21-m</i>	-3378.565	56.67	1.73 (Z-Γ)
orthorhombic	<i>Pmnb</i>	-3378.579	56.83	1.50 (Γ-Γ)
tetragonal	<i>P4-nmm</i>	-3378.562	57.15	0.66 (Z-Γ)
tetragonal	<i>P4-ncc</i>	-3378.562	57.02	0.71 (Γ-Γ)
triclinic	<i>P1</i>	-3378.607	56.71	1.34 (Γ-Γ)

<sup>a</sup> The final column indicates the location of the band gap.

**TABLE 2: Minimum and Maximum W-O Bond Lengths in Each Direction in Undeformed Crystalline Phases of WO<sub>3</sub><sup>a</sup>**

crystal	space group	W-O/Å		
		<i>x</i>	<i>y</i>	<i>z</i>
simple cubic	<i>Pm-3m</i>	1.902	1.902	1.902
monoclinic	<i>P21-c</i>	1.866–1.902	1.763–2.163	1.764–2.159
monoclinic	<i>P21-m</i>	1.865–1.937	1.785–2.087	1.759–2.166
orthorhombic	<i>Pmnb</i>	1.894	1.776–2.111	1.754–2.200
tetragonal	<i>P4-nmm</i>	1.897	1.897	1.730–2.336
tetragonal	<i>P4-ncc</i>	1.898	1.898	1.730–2.334
triclinic	<i>P1</i>	1.885–1.907	1.788–2.075	1.749–2.218

<sup>a</sup> Where only one distance is given, no bond length splitting occurs in that direction.

**TABLE 3: Literature Values for the WO<sub>3</sub> Volumes and Energies of Several Crystal Phases**

crystal	method	$E_{\text{WO}_3}/\text{eV}$	$\text{vol}_{\text{WO}_3}/\text{\AA}^3$	ref
simple cubic	GGA	-36.23	56.3	39
	LDA	-39.66	54.2	39
	LDA		56.6	42
	LDA		54.0	43
			54.01	44
	HF		53.37	41
	HF+corr		51.48	41
			56.62	55
	Expt.		53.15–53.37	45
	Expt.		50.65–51.27	46
tetragonal	Expt.		51.27	47
	Expt.		50.65–52.73	48
	GGA	-36.322	57.2	39
	Expt.		52.0	32
	exptl		54.0	35
	exptl		54.5	35
monoclinic R	GGA	-36.341	56.3	39
	LDA	-39.752	52.3	39
	exptl		52.96	30
monoclinic L	GGA	-36.336	55.8	39
	LDA	-39.751	52.7	39
	exptl		52.08	28
triclinic	GGA	-36.342	56.5	39
	exptl		52.74	24

Whereas the simple cubic structure contains W-O bonds of the same length in each direction, the tetragonal systems contain a splitting of bond lengths in one direction. Both the tetragonal *P4-nmm* and *P4-ncc* structures exhibit equal length W-O bonds in the *xy*-plane but splitting in the *z*-direction. The lattice volumes and W-O bond lengths are very similar for the two tetragonal systems, both unit cell volumes being slightly smaller than a previous GGA determination.<sup>39</sup>

The orthorhombic system exhibits alternation of long-short W-O bonds in both the *y*- and *z*-directions but not the *x*-direction. The triclinic and monoclinic phases contain W-O long-short splitting in all three directions. The splitting is strongest in the monoclinic systems due mainly to a strong W-O split in the *y*-direction. The *P21-c* structure shows greatest splitting in the *y*-direction. In the orthorhombic system splitting

**TABLE 4: Bandwidths for Seven Crystal Structures of WO<sub>3</sub><sup>a</sup>**

structure	bandwidths			
	W6s/meV	W6p/eV	O2s/eV	O2p/eV
<i>Pm-3m</i>	1.5 (Γ-R)	0.08 (X-M)	2.10 (Γ-R)	7.13 (M-R)
<i>P21-c</i>	2 (Γ-D)	0.18 (D-D)	1.88 (Γ-D)	6.78 (Γ-Z)
<i>P21-m</i>	23 (Y, Γ, B, A-Z, C)	0.18 (Z-Z)	1.95 (Γ-Z)	6.71 (Γ-Z)
<i>Pmnb</i>	34 (U-U)	0.19 (Γ-Γ)	1.90 (Γ-Γ)	6.85 (Γ-Γ)
<i>P4-nmm</i>	1 (Γ-Z)	0.23 (Z-A)	1.94 (Γ-Z)	7.13 (Z-Z)
<i>P4-ncc</i>	1 (Γ-Γ)	0.23 (Γ-M)	1.95 (Γ-Γ)	7.09 (Γ-Γ)
<i>P1</i>	12 (Γ-Γ)	0.80 (Γ-Γ)	1.92 (Γ-Γ)	6.90 (Γ-Γ)

<sup>a</sup> The location of the bandset is indicated by the symbols in parentheses.

in the *y*-direction is intermediate to the two monoclinic phases while splitting in the *z*-direction is larger than in the monoclinic phases though not as large as in the tetragonal phases. In the triclinic phase splitting in the *x*-direction is less than in either monoclinic phase, splitting in the *y*-direction is less than in any of the monoclinic or orthorhombic phases, and splitting in the *z*-direction is greater though not as great as in the tetragonal phases.

These four phases containing distortion in at least two directions possess similar lattice volumes, these being slightly smaller than in the tetragonal systems though at least 3% larger than in the simple cubic system. The predicted volumes for the monoclinic and triclinic phases are slightly larger than in a previous GGA calculation,<sup>39</sup> while no comparison for the orthorhombic phase is possible.

Similarities between the most distorted structures are also seen in the calculated ground-state energies, these being shown in Table 1. The triclinic phase is the deepest in energy, followed by the orthorhombic and monoclinic phases. The near isoenergetic nature of these phases is consistent with the observation of a broad metastability domain in this material. Both tetragonal phases are a few meV higher in energy than the more distorted structures with the simple cubic phase a further 0.14 eV higher. The relative energies of these phases show good agreement with those of previous GGA calculations<sup>39</sup> shown in Table 3. We do, however, find that the monoclinic and tetragonal phases are relatively lower in energy and closer together with the position of the monoclinic phases reversed. This is not considered as of importance since the structures are slightly different and LDA calculations find no more than 1 meV between the phases. It is worth noting that an accurate prediction of the thermal phase ordering of these polymorphs would require computation of the configurational entropy for each phase, and is considered beyond the scope of this work.

**1. Simple Cubic *Pm-3m*.** The band structure shows several features that may be briefly summarized. W6s states are located at roughly 75 eV below the Fermi level, W6p bands are located at roughly 39 eV below the Fermi level, O2s bands are located at 16–18 eV below the Fermi level, and the O2p bands are located between around 7 eV below the Fermi level and the Fermi level, these forming the valence band. It will soon be shown that mixing of levels renders the above assignment of band sets inaccurate though for the sake of convenience this nomenclature is used throughout. The bandwidths for all seven crystals under study are given in Table 4 with band gaps given in Table 1. The width of the valence band closely matches the 7.0 eV predicted in two earlier studies.<sup>39,55</sup>

The charge density associated with the O2p bands is shown in Figure 1. The deepest bands are bonding O2p states. Intermediate energy bands show mixing with W5d states and significant hybridization, the middle band showing equal



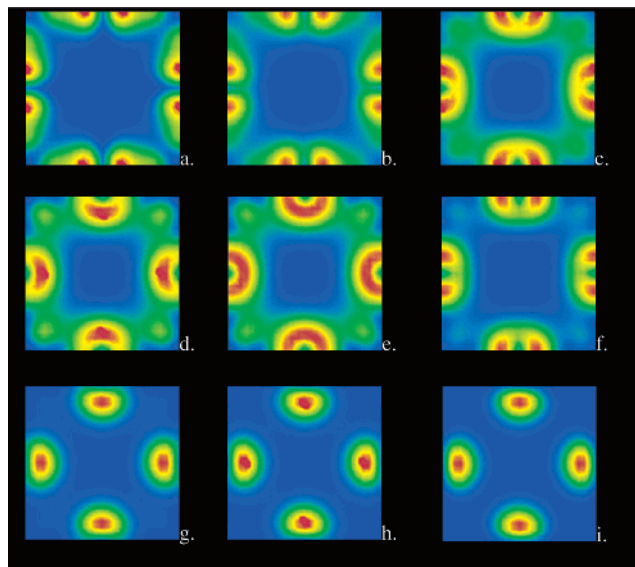


**Figure 1.** Electron density of the valence bands in simple cubic WO<sub>3</sub> in order of energy, (a) being lowest and (i) being highest.

contributions from bonding and antibonding O2p components. The highest energy bands are entirely antibonding O2p in nature.

A comparison of computed band structures between this work and earlier work<sup>39</sup> at the GGA level of theory shows generally good qualitative agreement. Minor differences are that we find the top of the valence band to lie at the R point where the previous work found all points on the trajectory between the M and R points of the Brillouin zone to be equal in energy. This work also finds that the bottom of the conduction band is at the  $\Gamma$  point whereas the previous work found this to be all points along the X– $\Gamma$  trajectory. The indirect gap of 0.69 eV (R– $\Gamma$ ) is a significant improvement over the 0.4 eV predicted in an earlier work and our prediction of finite dispersion at the top of the valence band and bottom of the conduction band is in agreement with all-electron calculations.<sup>21</sup> Given the link between density and band gap, carefully studied in the previous GGA work, a larger band gap is to be expected for the smaller lattice volume obtained herein. The difference in the location of the top of the valence band and bottom of the conduction band may be attributed to differences in the pseudopotential. The treatment of the pseudopotential is the major difference between the results presented here and those of the earlier GGA work.<sup>39</sup> The construction and use of a nonlocal pseudopotential incorporating W6s and W6p states as valence states clearly has a strong effect on the density and band gap predictions. The changes in and effect of the W6s and W6p states are more clearly seen in distorted systems so the pseudopotential is discussed further later.

The lowest energy bands in the conduction band are due mainly to W5d. A small contribution from O2p is also noted in the conduction band, this being similar to the conduction band in ReO<sub>3</sub> where the lowest bands are antibonding states composed of O2p and W5d.<sup>56</sup>

Population analysis predicts that the charge state of the ions is W<sup>5.78+</sup> and O<sup>1.93–</sup>, this being consistent with the presence of W5d components in the valence band and O2p components in the conduction band. Importantly, this implies covalency and the purely ionic picture of W<sup>6+</sup> and O<sup>2–</sup> ions is not predicted. Interestingly the population analysis also reveals that the electron depletion on O ions is in part due to loss of p electrons and in part due to loss of s electrons. This finding may be explained

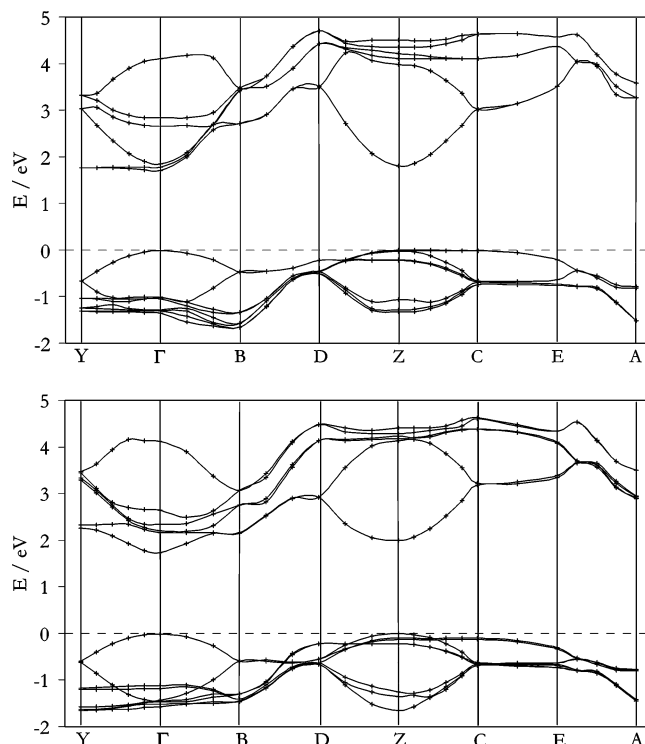


**Figure 2.** The band structure around the Fermi level for P21-c (top) and P21-m (bottom) monoclinic WO<sub>3</sub>.

in terms of sp<sup>3</sup>d<sup>2</sup> hybridization and contradicts the common understanding of WO<sub>3</sub> being a d<sup>0</sup> material.

**2. Monoclinic P21-c and P21-m.** The W6s states in the P21-c system show very little difference to those in the simple cubic system though the W6p bandwidth is doubled. In contrast to this behavior, the O2s and O2p bandwidths are both compressed relative to the simple cubic system. The highest valence band consists of both p<sub>x</sub> and p<sub>y</sub> antibonding components centered on O ions. The p<sub>y</sub> components of this band display merging in the z-direction, this giving a distorted toroidal structure in the yz-plane, similar to the intermediate energy O2p bands in the simple cubic system. Antibonding p<sub>x</sub> components are also present on oxygen bonded in the z-direction. Pure p-bands are deeper in energy. The bandstructure around the Fermi level is shown in Figure 2 for both monoclinic phases.

The lowest unoccupied bands located at  $\Gamma$  have 3-fold degeneracy and these are shown in Figure 3a–c. The predicted band gap is 1.71 eV between Z and  $\Gamma$  though the highest valence band is only 0.02 eV lower in energy at  $\Gamma$  and the lowest unoccupied band is only 0.01 eV higher in energy at Z, this band being shown in Figure 3d. The lowest energy conduction band at  $\Gamma$  is composed of both p<sub>x</sub> centered on O ions in the xy plane containing both W and O, and d lobes centered on W. These W5d lobes all show merging in the z-direction and half of the lobes are merged in the y-direction. The lowest conduction band at the Z point is quite different, though it is again composed of both p and d components. The p component is mainly p<sub>x</sub> centered on those O ions out of the W–O xy plane and shows merging in the y-direction. The d components of this band, centered on W, are merged in the x- and y-directions but show no merging in the z-direction.

The P21-m system is similar to the P21-c in terms of the structural parameters and ground-state energy though significant differences are found in the band structure. In this system the W6p bandwidth is the same as in the P21-c system though the W6s bandwidth is an order of magnitude larger. The O2s

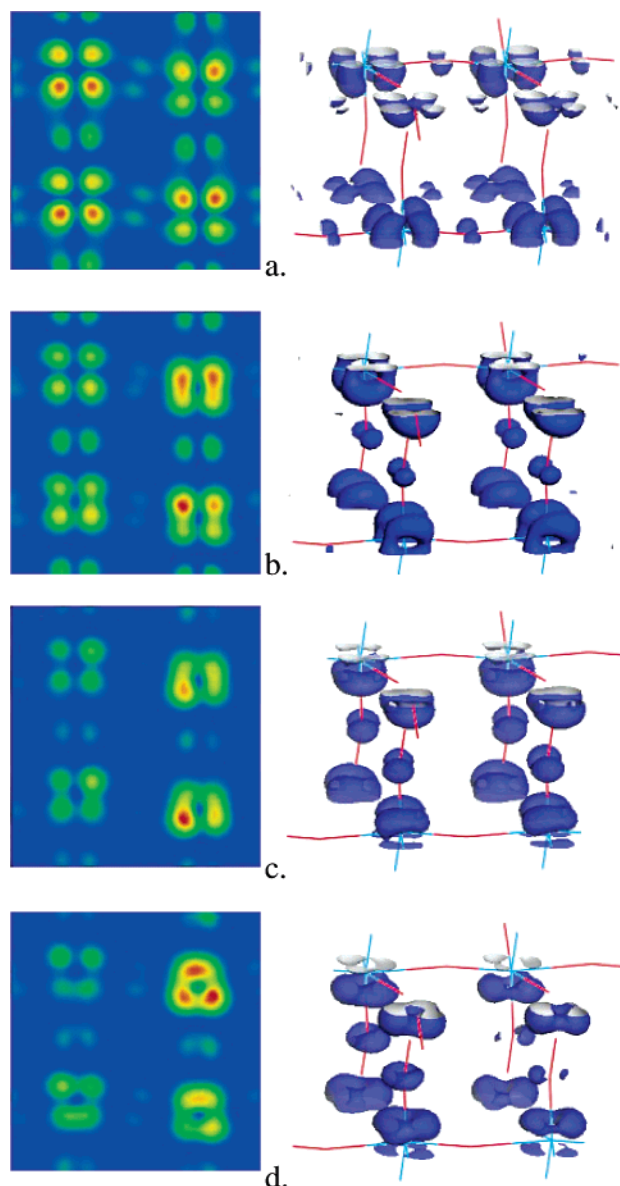


**Figure 3.** The four lowest conduction bands in *P21-c* monoclinic  $\text{WO}_3$  increasing in energy from a to d.

bandwidth is compressed relative to the simple cubic system but not as much as in the *P21-c* system, which shows the greatest O2s compression among the systems under study. The O2p bandwidth is most compressed in the *P21-m* system. The highest W6p, lowest and highest O2s, and lowest O2p bands all show little dispersion across the  $\text{Y}-\Gamma$  trajectory. The top of the valence band lies at Z though it is only 0.01 eV lower in energy at  $\Gamma$ . The composition of the highest valence band is similar to that in *P21-c* though only half of the  $xz$ -planes contain any  $p_x$  centered on O. It is only on these planes containing  $p_x$  that merging of the d lobes occurs in the  $y$ -direction.

The top few valence bands show significant splitting of levels, as shown in Figure 2, with different splitting at Z and  $\Gamma$ . The lowest conduction band is lowest in energy at the  $\Gamma$  point, and also differs from the *P21-c* system in a similar way to the highest valence band. Full  $yz$  merging of d-lobes occurs in the same place as in the highest valence band and elsewhere only  $z$  merging is observed.

An indirect band gap of 1.73 eV between Z and  $\Gamma$  is predicted and in a similar way to the *P21-c* system the  $\Gamma-\Gamma$  gap is only 0.01 eV larger. The existence of an indirect gap is in agreement

with experiment<sup>57</sup> and in contradiction to previous GGA calculations.<sup>39</sup> The direct gap of 0.90 eV (GGA), 1.1 eV (LDA) predicted by the previous work has clearly been improved upon and good agreement is found with the 1.68 eV gap predicted by that work for experimentally determined atomic positions as opposed to correctly relaxed structures. When taking into account the well-known underestimation of band gaps in DFT, good agreement is found between our band gap for a fully relaxed structure and that found in experiment.

The decrease in O2p bandwidth for both monoclinic systems may be attributed to the existence of long-short W-O splitting in all three directions:  $\text{W}5d_{yz}$  overlaps with  $\text{O}2p_y$  and  $\text{O}2p_z$ ,  $\text{W}5d_{xz}$  overlaps with  $\text{O}2p_x$  and  $\text{O}2p_z$ , and  $\text{W}5d_{xy}$  overlaps with both  $\text{O}2p_x$  and  $\text{O}2p_y$ . A decrease in bandwidth reflects decreased overlap and decreased bonding/increased antibonding. Long-short splitting in the  $xy$  plane is less than in the  $z$  direction though the resultant bonding-antibonding interaction causes a drop in energy in the valence states and an increase in the energy of conduction states. The result of both bandsets moving is a large increase in band gap over the simple cubic system. The effect of this splitting on the band structure is shown in Figure 2 for both monoclinic structures.

**3. Tetragonal *P4-nmm* and *P4-ncc*.** In both *P4-nmm* and *P4-ncc* phases the Ws bandwidth is smaller than in the simple cubic phase. The W6p bands are split into two sets for both tetragonal systems. The lower set comprises two bands that are degenerate at M and X, and at A and R. The upper set of W6p bands is also comprised of two bands, these being degenerate and near dispersionless along R-X. The degeneracy is lifted at all other points (Z, A, M,  $\Gamma$ ) with splitting of the order of 0.04 eV and it appears as though the degeneracy is also present at the midpoint along the Z-A and M- $\Gamma$  trajectories. The uppermost of these bands show near degeneracy at the  $\Gamma$  and Z points. The O2p bandwidth is similar to that in the simple cubic system, this being in contrast to previous GGA findings<sup>39</sup> that suggested compression of these bands, though the similar band gaps in *P4-nmm* and *Pm-3m* systems is in agreement with this earlier work. The bottom of the conduction band is in the same location with  $\Gamma$  laying only 2 meV below Z.

The top valence band is composed of  $p_x$  and  $p_y$  centered on O ions in the W-O bonding  $xy$ -plane, these being merged in the  $z$ -direction. This band is also composed of  $p_x$ ,  $p_y$  on the O ions out of the W-O bonding  $xy$ -plane, evidenced by toroidal shaped charge density isosurfaces. The lowest conduction band is also comprised of these  $p_x$ ,  $p_y$  toroids and  $p_x$  and  $p_y$  in the W-O  $xy$ -plane though these latter p components are not merged in the  $z$ -direction, as they are in the highest valence band. The lowest conduction band also contains d components centered on the W ions, merged in all three directions.

The structure of the highest valence bands and lowest conduction bands can be explained in terms of the displacement of W ions in opposite directions, this allowing an overlap of  $\text{W}5d_{yz}$  with  $\text{O}2p_y$  and  $\text{W}5d_{xz}$  with  $\text{O}2p_x$ . Since there is no relative displacement of the W ions in the  $xy$ -plane there is no such overlap of  $\text{W}5d_{xy}$  with any O2p component.

In the *P4-ncc* phase there are again two distinct W6s band sets, degenerate at the A and R points, split into two sets at the M, Z, and X points with four distinct bands at  $\Gamma$  and all points along  $\Gamma-X$ ,  $\Gamma-M$ , and  $\Gamma-Z$ . The deeper of the W6p sets displays the same level splitting as the W6s levels though with no bandcrossing. The upper set shows the same features as the *P4-nmm* structure except there is a slight splitting of 1 meV at the M,  $\Gamma$ , and X points. Both the highest and lowest O2p bands at  $\Gamma$  are split from degenerate bands at Z within 1 meV and

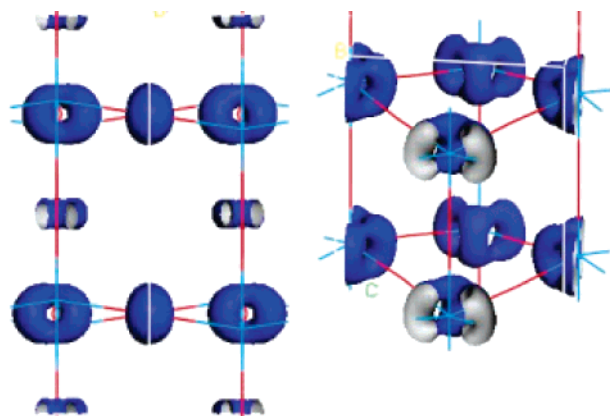


**Figure 4.** The highest valence band (left) and lowest conduction band (right) in *P4-ncc* WO<sub>3</sub>.

similar behavior is noted for the lowest conduction band. The highest valence band is composed of antibonding states on O and the lowest conduction band is composed of antibonding states centered on W as shown in Figure 4. The top valence band appears very similar to that in the *P4-nmm* system and all bandwidths are also similar. A slightly larger O2p bandwidth is noted in the *P4-nmm* system indicating increased bonding in this system. The lowest conduction band is composed of W-centered d-lobes merged in all directions, as seen in the *P4-nmm* system though no p components centered on O ions are present in *P4-ncc* WO<sub>3</sub>.

**4. Orthorhombic *Pmnb*.** The W6s bandwidth is largest in the orthorhombic system and the O2s bandwidth is intermediate to the two monoclinic systems. The W6p and O2p bandwidths are compressed relative to the tetragonal and simple cubic structures though slightly larger than in the monoclinic systems.

The highest energy valence levels are predominantly p-states on the oxygen ions though some minor mixing with W5d states is noted. The lowest unoccupied level in the conduction band is mainly W5d though it also contains O2p. The band gap of 1.50 eV is direct and located at  $\Gamma$ . The band gap at Z is only 0.03 eV larger and these lowest conduction and highest valence bands show negligible dispersion over the  $\Gamma$ –Z trajectory. The band gap is larger than the simple cubic (splitting in 0-directions) and tetragonal (splitting in one direction) systems though not as large as in monoclinic systems (splitting in three directions).

**5. Triclinic *P1*.** The W6s and O2s bandwidths are intermediate to the two monoclinic systems though the W6p and O2p bandwidths are slightly larger. The O2s and O2p bandwidths are very similar to those in the orthorhombic system though slightly larger. All bandwidths are between  $\Gamma$  and  $\Gamma$ . The band gap of 1.34 eV is also at  $\Gamma$  with all points along  $\Gamma$ –Z being near degenerate. The Z–Z band gap is 0.04 eV larger. The highest valence band consists of antibonding  $p_y$  located on O ions in the  $xz$ -plane and antibonding  $p_x$  located on O ions in the  $yz$ -plane. The  $p_x$  components show slight distortion in the  $z$ -direction. The lowest conduction band is almost entirely 5d<sub>xy</sub> though some mixing with O2p is noted. The slightly increased O2p bandwidth with respect to the orthorhombic system indicates less bonding–antibonding interaction and this is reflected in the difference in band gaps.

**6. Summary of Undefected WO<sub>3</sub> Phases.** The electronic structures of the pure WO<sub>3</sub> phases may be readily interpreted in terms of long–short W–O bond splitting. The relationship between the shortest W–O bond in the  $x$ -,  $y$ -, and  $z$ -directions and band gap is shown in Figure 5. For the simple cubic system, where no splitting occurs, a relatively small band gap is

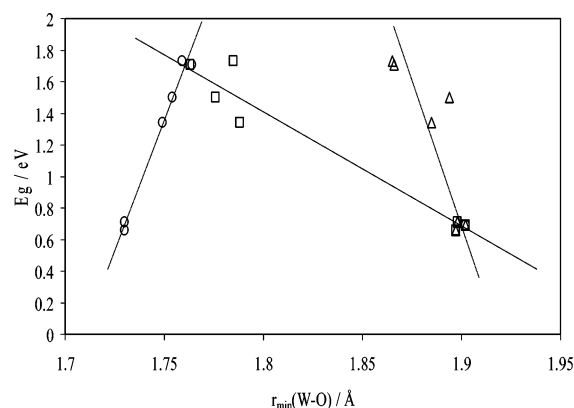


**Figure 5.** The effect of W–O bond length splitting on the band gap of WO<sub>3</sub> in terms of the shortest bond in any direction ( $x$ , triangles;  $y$ , squares;  $z$ , circles). Lines are merely a guide to behavior.

predicted between  $x$  and  $y$  components of O2p and W5d. Tetragonal systems show strong W–O splitting in the  $z$ -direction only, though bonding–antibonding interactions in this direction do not affect the  $x$  and  $y$  components either side of the gap and so the band gap remains unchanged from the simple cubic system. The orthorhombic system shows fairly strong splitting in the  $z$ -direction and also splitting in the  $y$ -direction. Bonding–antibonding interactions in the  $y$ -direction cause a drop in the energy of O2p<sub>y</sub> components and a raising of W5d<sub>xy</sub> and W5d<sub>yz</sub> resulting in an increased band gap. Monoclinic systems show W–O splitting in all three directions, with splitting in the  $x$ - and  $y$ -directions being the most significant among the systems under study. Resulting bonding–antibonding interactions cause a large increase in the band gap. The triclinic system also shows splitting in all three directions though much of this is confined to the  $z$ -direction. Splitting in the  $x$ -direction is small and splitting in the  $y$ -direction is less than that in the orthorhombic and monoclinic systems. The presence of W–O bond splitting causes an increase in the band gap though the magnitude of the splitting in the important  $x$ - and  $y$ -directions means that the band gap does not increase as much as in the monoclinic or orthorhombic systems.

The magnitude of the band gap in these materials is dominated by splitting in the  $y$ -direction with increased splitting resulting in shorter W–O bonds, increased overlap, increased bonding–antibonding interaction, and a wider gap. Splitting in the  $x$ -direction has a similar effect though to a lesser extent while splitting in the  $z$ -direction has the opposite effect: Shorter W–O bonds in this direction tend to decrease the magnitude of the O2p–W5d gap. The splitting is evident in all bandwidths with increased  $y$ -splitting causing an increase in the widths of W6s and W6p and decrease in the widths of O2s and O2p. This is due to bonding–antibonding interactions that lower the energy of O2p<sub>y</sub> components. The largest magnitude of the band gap is associated with increased antibonding in the W6s and W6p states and increased bonding in the O2s and O2p states. The nature and location of the hybrid states that form in the O2p and W5d bands,  $e_g$  and  $t_{2g}$  in a nonlocal description or  $sp^3d^2$  in a local description, are critically dependent upon the overlaps. Clearly the inclusion of W6s and W6p in the valence wave function calculation will affect the energy and location of the hybrid states, this in turn affecting the computed band gap. Choices made in constructing the pseudopotential must be made very carefully given the strength of the effects on the calculated electronic structure. The improved predictions for the volume of the simple cubic phase, first realistic DFT–GGA band gaps, and predicted dispersion characteristics in agreement with all-



**TABLE 5: Unrelaxed and Relaxed Vacancy Formation Energies for the Seven Phases of WO<sub>3</sub> under Study<sup>a</sup>**

crystal	space group	<i>nW</i>	<i>E</i> <sub>Ovac</sub> /eV	
			unrelaxed	relaxed
simple cubic	<i>Pm-3m</i>	8	4.23	3.30
monoclinic	<i>P21-c</i>	4	5.46	4.53
		8 <sup>b</sup>		4.41
		8 <sup>c</sup>		3.46
monoclinic	<i>P21-m</i>	4	5.34	4.51
orthorhombic	<i>Pmnb</i>	8	5.47	4.88
tetragonal	<i>P4-nmm</i>	16	9.18	3.83
tetragonal	<i>P4-ncc</i>	16	4.81	3.37
triclinic	<i>P1</i>	8	5.69	4.91

<sup>a</sup> *nW* is the number of W atoms in the unit cell. <sup>b</sup> Unit cell doubled in the *x*-direction. <sup>c</sup> Unit cell doubled in the *y*-direction.

electron calculations give confidence in the ability of our pseudopotential as we extend its use to defected systems.

**B. The Oxygen Vacancy in WO<sub>3</sub>.** Due to the use of periodic boundary conditions, and the need to keep computational systems as small as possible, in the 32-atom cells (*nW* = 8) a single O ion separates the two W ions in the direction away from the vacancy. This bridging O ion is only absent in the tetragonal systems where the unit cell, which is rotated through 45° relative to the other systems, required further expansion to reach a vacancy–vacancy distance of at least two W–O bonds. This was the motivation for choosing the large 64-atom cell for studying the vacancy in the tetragonal system as opposed to the 32-atom cells used elsewhere. The oxygen vacancy in the monoclinic *P21-c* system has been studied in both a 16-atom cell, due to the observation of stable W<sub>4</sub>O<sub>11</sub> clusters,<sup>58</sup> and 32-atom cells of varied geometry, due to the need to standardize findings. The degree of substoichiometry in the systems studied is compatible with the region of importance to chromism mechanisms in WO<sub>3-*y*</sub>, i.e., the change between *y* < 0.3 and 0.3 < *y* < 0.5. The systems of size *n* = 4, 8, 16 correspond to W<sub>4</sub>O<sub>11</sub> (*y* = 0.25), W<sub>8</sub>O<sub>23</sub> (*y* = 0.125), and W<sub>16</sub>O<sub>47</sub> (*y* = 0.0625), respectively.

The effect of cell size is in fact the effect of vacancy–vacancy interaction and validation of the choice of system sizes can be seen from the unrelaxed and relaxed vacancy formation energies, as shown in Table 5. The effect of an oxygen vacancy in a 16-atom (*nW* = 4) cell of *P21-c* symmetry is to create a periodic stack of vacancies such that an extended defect, a channel of unoccupied volume, forms. The effect of removing the channel of vacancies is to lower the vacancy formation energy from ~4.5 eV to ~3.5 eV, while doubling the size of the monoclinic cell in the other directions, while retaining the vacancy channel lowers the vacancy formation energy by only ~0.1 eV. The behavior of the 64-atom tetragonal systems is therefore very similar to that of the 32-atom cells and it would be expected that a hypothetical 32-atom cell vacancy formation energy would be less than 0.1 eV above the value found in the 64-atom cell. This allows a comparison between the oxygen vacancy formation energy in various cell geometries to be made.

The oxygen vacancy formation energy appears highest in the triclinic and orthorhombic phases at just under 5 eV. The formation energy in *P4-nmm* tetragonal WO<sub>3</sub> is ~3.9 eV when correcting for the vacancy interactions. In the *P4-ncc* phase and both monoclinic phases the formation energy is ~3.4–3.5 eV. The low vacancy formation energy, 3.3 eV, in the simple cubic system reflects the low relative stability of the bulk phase: The introduction of a vacancy provides the symmetry breaking necessary for the lifting of the 2nd-order Jahn–Teller instability in this phase.

Lattice distortion is an important component of a polaron and the energy associated with this distortion may be estimated from the difference in energy between unrelaxed and relaxed vacancy systems. This is ~0.6 eV in the orthorhombic system, ~0.8 eV in the triclinic system, and ~0.9 eV in the cubic system. The *P21-m* relaxation energy is ~0.8 eV and that of *P21-c* is ~1.0 eV though these relate to smaller polarons. The large relaxation energy in the *P4-ncc* system is ~1.4 eV though this relates to a larger polaron where a less strained relaxation can occur. For the same reason, the relaxation energy in the monoclinic systems should be expected to be higher than that in the cubic system. This explanation leaves the single anomaly of the very large unrelaxed vacancy formation energy in the *P4-nmm* system, ~5.3 eV, which will be explained in section B.3.

In each case the relaxation around the vacancy involves an increase in the W–W distance across the vacancy and an associated shortening of W–O bonds on these W ions. The degree of bond shortening, given in Table 6, was shown to be of great importance in the undefected structures and is discussed in terms of the electronic structures of defected systems in the following sections.

*1. Simple Cubic Pm-3m.* The bridging W–O bond length in the *x*-direction decreases from 1.902 Å to 1.792 Å. Other bonds within the *xy*-plane show minor splitting in the *x*-direction with bond lengths in the range 1.885–1.918 Å though no splitting in the *x*-direction is noted in the *xy*-plane with no vacancy. Splitting in the *y*-direction is more pronounced at 1.868–1.947 Å in the plane of the vacancy and 1.892–1.912 Å on the defect-free *xy*-plane. Splitting in the *z*-direction is 1.868–1.946 Å.

Upon relaxation, the oxygen vacancy induces splitting of the W6s levels. Eight W ions are present in the 2 × 2 × 2 cell studied and for this geometry four doubly degenerate spin-paired bands are noted. The deepest levels reside on the W ions separated by the oxygen vacancy with the next deepest levels, 0.30 eV higher in energy, residing on the next nearest W ion, this lying out of the oxygen vacancy plane. A set of bands residing on the next-nearest W ions, within the oxygen vacancy plane, is a further 0.13 eV higher in energy and the highest set of W6s levels reside on those W ions furthest from the vacancy and are a further 0.06 eV higher in energy.

The deepest set of W6p levels are centered on W ions adjacent to the vacancy with higher sets being located on progressively distant W ions as with the W6s levels. Within each set of these levels p<sub>y</sub> states are deepest followed by p<sub>z</sub> then p<sub>x</sub> states. An exception to this ordering is noted for the antibonding p<sub>x</sub> states on the second nearest neighbor and more distant W ions. Spatially these states appear toroidal and are identifiable by a lack of dispersion. The lower of these two dispersionless bands lies near to the top of the energy range of the deeper bands while the second band lies 0.1 eV above these bands and 0.1 eV below the next set. The middle set of W6p bands is very similar to the bottom set in ordering except that the dispersionless p<sub>x</sub> bands overlap in energy with the other components and some spin uncoupling is observed. The uppermost set of bands is again similar though this time the dispersionless bands are located within and below the other levels. The two levels within the dispersionless set off the bottom show spin uncoupling. The complete bandwidth of the W6p bands is 0.62 eV (Γ–Γ).

A single spin-paired O2s band, which is dispersionless, lays some 0.45 eV below the other O2s bands. This s orbital is located on the O ion joining the two W ions adjacent to the vacancy. A small amount of p centered on W is also noted for this level. The remainder of the O2s levels remain essentially unchanged from the undefected system with a bandwidth of

**TABLE 6: Bandwidths and O2p–W5d Gap for Seven Crystal Phases of WO<sub>3</sub> Containing an Oxygen Vacancy<sup>a</sup>**

structure	bandwidths/eV				gap/eV O2p–W5d
	W6s	W6p	O2s	O2p	
<i>Pm-3m</i>	0.46 (Γ–Γ)	0.62 (Γ–Γ)	2.59 (Γ–Γ)	7.12 (Γ–Γ)	0.75 (Γ–Γ)
<i>P21-c</i>	0.07 (Y, A–D, Z, C, E)	0.45 (Γ, B–B, A)	2.50 (Γ–Z)	7.02 (Y–D) <sup>2</sup>	1.36 (D–A)
	0.04 (D, Z–Z)	0.41 (D–C, Z)	2.53 (Γ–D, Z)	6.94 (Y–D)	1.14 (D–A)
<i>P21-m</i>	0.002 (Γ–Z)	0.18 (Z–Z)	1.86 (Γ–Γ)	6.74 (Γ–Z)	2.00 (Z–Γ)
<i>Pmnb</i>	0.70 (all points)	0.86 (Γ, Z, X, U–Γ)	2.10 (Γ–Γ)	7.10 (Γ–Γ)	1.14 (Γ, Z–Γ)
<i>P4-nmm</i>	0.27 (A–A)	1.18 (Z–A)	2.68 (Γ–A)	7.84 (Γ–Z)	0.52 (Z–Γ)
	0.28 (A–R)	1.09 (Z–X)	2.67 (Γ–A)	7.84 (Γ–Z)	0.53 (Z–Γ)
<i>P4-ncc</i>	0.70 (X–R)	1.12 (Z–A)	2.43 (R–Z)	7.78 (Γ–R)	0.52 (R–Γ)
	0.71 (X–A)	1.15 (Z–A)	2.64 (Γ–Z)	7.78 (Γ–Z)	0.53 (Z–Γ)
<i>P1</i>	0.59 (all points)	2.75 (Γ–Γ)	2.35 (Γ–Γ)	7.08 (Γ–Γ)	1.10 (Γ–Γ)
	0.51 (all points)	2.57 (Γ–Γ)	2.36 (Γ–Γ)	7.08 (Y–Γ)	1.05 (Γ–Γ)

<sup>a</sup> The symbols in parantheses following the width/gap indicate the location of the bandset. Where two values are given these are for the different spin components.

2.14 eV (Γ–Γ). Including the isolated dispersionless band the O2s bandwidth becomes 2.59 eV (Γ–Γ). As with the other bands, the deepest levels are those that correspond to locations close to the defect.

The O2p bandwidth is 7.12 eV (Γ–Γ) with the highest energy at  $E_F - 1.72$  eV. A 0.75 eV (Γ–Γ) gap separates the top of the O2p band and the bottom of the W5d band. The lowest bands of the W5d levels cross the Fermi level so the system is metallic, as in fact are all of the oxygen deficient systems studied herein. The excess electrons due to oxygen removal are located in the lowest W5d bands. These are all mainly W5d<sub>yz</sub> in nature though minor mixing with O2p is noted. The lowest level comprises connected d<sub>yz</sub> lobes and isolated O2p. The next few higher bands are very close energetically and show a tendency for the O2p component to disappear and for the d-lobe connection to become more pronounced. The slight increase in the gap between the O2p and W5d states can be attributed to bonding–antibonding splitting as in the pure systems and the metallicity is in agreement with experimental observations.<sup>6</sup>

2. *Monoclinic P21-c and P21-m.* For the *P21-c* system W–O bonds in the *y*-direction range from 1.808 to 1.829 Å for the bridging O and 1.813–2.144 Å elsewhere. Splitting in the *x*-direction ranges from 1.849 to 1.933 Å and splitting in the *z*-direction ranges from 1.783 to 2.135 Å. Compared to the undefected system, splitting is increased in the *x*-direction but decreased in the *y*- and *z*-directions.

Level splitting of the W6s states is also noted upon introduction of a vacancy in the *P21-c* structure. The W6s bandwidth increases to 0.30 eV. The bands are arranged with a set of four bands within 70 meV with the corresponding bands of opposite spin appearing 0.26 eV above. Substantial spin uncoupling also occurs within the W6p bands. The lowest band for a particular spin corresponds to a p<sub>y</sub> located on the W ions adjacent to the vacancy. The next lowest band consists of p<sub>y</sub> on these atoms but also distorted p<sub>y</sub> on other W ions. As higher energy bands are considered the orbitals correspond to p<sub>z</sub> then p<sub>x</sub>, and then p<sub>z</sub>, p<sub>y</sub>, and p<sub>x</sub> on W ions increasingly distant from the vacancy. The gap between the bands for the different spins is roughly 0.29 eV.

As with the simple cubic structure containing a vacancy, a single Os band resides below the others this being associated with s on the O ion that bridges the W ions adjacent to the vacancy. Increases in energy with going from p<sub>y</sub> to p<sub>z</sub> to p<sub>x</sub> are again noted as is the effect that higher energy bands are associated with ions further from the vacancy. The total O2s bandwidth is 2.56 eV reflecting a ~0.03 eV offset between the two spin-components.

The O2p levels display the same ordering as in simple cubic though some spin-splitting is noted. The low-energy O2p band

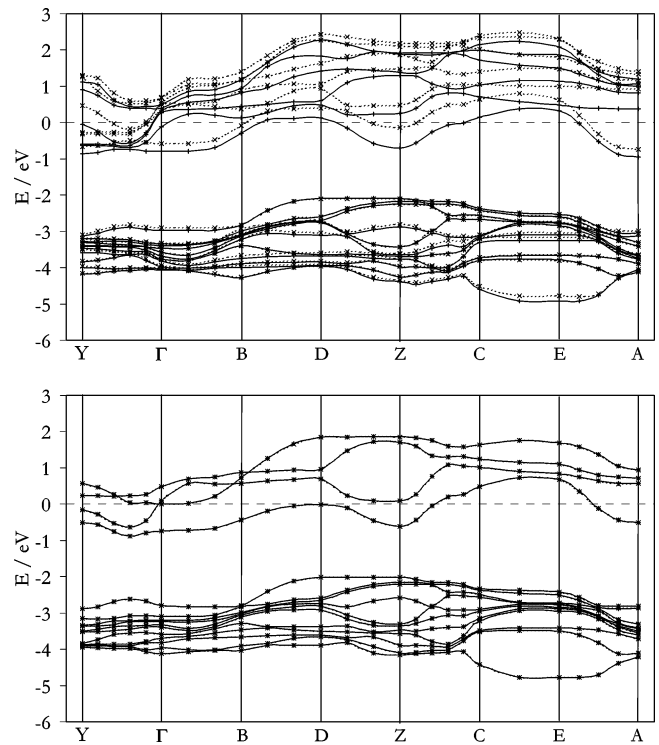


**Figure 6.** The band structure around the Fermi level for *P21-c* (top) and *P21-m* (bottom) monoclinic WO<sub>3</sub> containing an oxygen vacancy. The two spin components are represented by solid and dashed lines.

at Y is nearly dispersionless along Y–Γ and the high-energy O2p band at D is nearly dispersionless along D–Z. The large spin splitting seen in the O2p–W5d gaps is due to splitting of the d levels that cut the Fermi level as shown in Figure 6. The lowest W5d bands all contain amounts of O2p and display d-lobe merging, the extent of which increases with band energy. These states are shown in Figure 7a–d. The decrease in the O2p–W5d gap corresponds to the decreased bonding–antibonding interaction due to decreased W–O splitting in the *y*-direction.

For the *P21-m* system W–O bond splitting in the *x*-direction is 1.833–1.972 Å, in the *y*-direction it is 1.822–1.841 Å on the bridging oxygen and 1.858–2.047 Å elsewhere, and in the *z*-direction it is 1.759–2.160 Å. As in the *P21-c* system, splitting is increased in the *x*-direction but decreased in the *y*-direction. The shortest W–O bond in the *z*-direction remains unchanged from that of the undefected crystal system.

The effects of a vacancy on the bandwidths in this phase are quite unusual. The W6p bandwidth is unchanged upon introduction of an oxygen vacancy while the W6s and O2s bandwidths



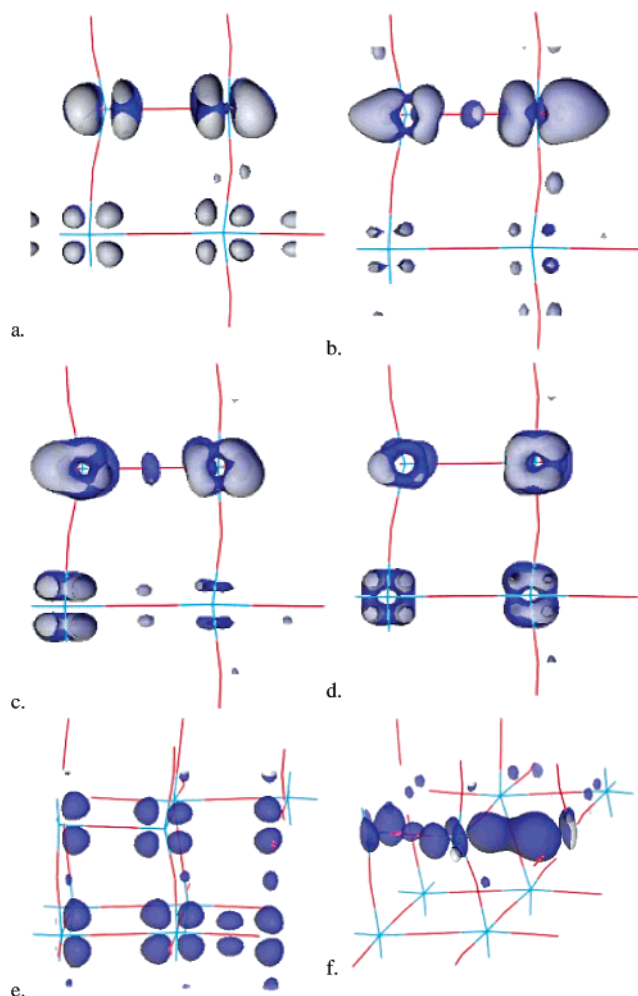


**Figure 7.** The four lowest W5d levels in *P21-c*  $\text{WO}_3$  with an oxygen vacancy (a–d) and the two spin components of the lowest W5d level in *P1*  $\text{WO}_3$  with an oxygen vacancy (e, f).

are compressed. Additionally, the O2p–W5d gap increases. The highest O2p band shows Op–Wd mixing, as does the lowest W5d band, this being occupied and crossing the Fermi level. The increase in the gap between the O2p and W5d states may be attributed to an increased bonding–antibonding interaction in the *x*-direction, evidenced from increased W–O splitting in this direction.

Two significant differences between the oxygen deficient monoclinic systems is the spin-uncoupling and decrease in the energy of the lowest W5d state at the A-point in the *P21-c* system. These effects are clearly seen in Figure 6, which compares the bandstructures near the Fermi level for the two monoclinic structures containing an oxygen vacancy.

In the *P21-m* system the O2p bands are located at  $\Gamma$ –Z and the lowest W5d state is at the  $\Gamma$ -point in both undefected and defected systems. In the *P21-c* system the O2p bands are also located at  $\Gamma$ –Z and the lowest W5d state also appears at  $\Gamma$ ; however, the defect substantially changes the location of these states. The O2p bands are located at Y–D with the lowest W5d band at the A-point. Excess electrons are located in this non-spin-degenerate band at A.

**3. Tetragonal *P4-nmm* and *P4-ncc*.** Relaxation of the atomic positions around a vacancy in *P4-nmm*  $\text{WO}_3$  induces splitting in the *x*- and *y*-directions of 1.745–1.999 Å and in the *z*-direction of 1.736–2.317 Å.

Spin-uncoupling of levels is also noted in this defected structure: The W6s levels have a total bandwidth of 0.29 eV

(A–R) though one spin component has a bandwidth between A–A and is offset by 0.01 eV. As with previously discussed systems a single O2p level lies below the other levels, this being associated with the oxygen atom bridging the W ions adjacent to the oxygen vacancy. This band is separated by the main set of O2p bands by 0.15 eV for one spin and 0.18 eV for the other spin, both being direct at A. The very small O2p–W5d gap and large O2p bandwidth are indicative of large bonding contributions.

In the *P4-ncc* system, W–O bond length splitting upon introduction of a vacancy is 1.747–1.999 Å in the *x*- and *y*-directions and 1.726–2.398 Å in the *z*-direction. This corresponds to an induced splitting in the *x*- and *y*-directions in the same way as was noted for the *P4-nmm* system. However, in the *P4-ncc* structure a slight increase in splitting in the *z*-direction is noted upon introduction of a relaxed vacancy.

Significant spin uncoupling is again noted throughout the band structure. In common with the previous tetragonal structure the W6s levels are spin-split with the highest band located at A for one spin and R for the other. The lowest O2s levels also appear at different locations, R and  $\Gamma$ , for the two spin components. An O2p band associated with the bridging oxygen ion is again evident in this structure, this having a bandwidth of 0.25 eV ( $\Gamma$ –A) for both spins, and laying 0.20 eV below the main set of O2p bands. The total O2p bandwidth is 7.78 eV for both spin components though the highest bands are located at R and Z for the two spin components. The O2p–W5d gap is therefore in a different location for the two spin components, one being 0.52 eV (R– $\Gamma$ ) and the other 0.53 eV (Z– $\Gamma$ ). As with the *P4-nmm* system the large O2p bandwidth and small gap are indicative of large bonding contributions.

In the *P4-nmm* system the location of the O2p–W5d gap is Z– $\Gamma$  in both undefected and defected systems. In the *P4-ncc* system the lowest W5d band appears at the  $\Gamma$ -point in both undefected and defected systems though the location of the highest O2p band changes from  $\Gamma$  to R for one spin and Z for the other spin. Excess electron states are, however, located at  $\Gamma$  for both defected systems.

The large unrelaxed vacancy formation energy in the *P4-nmm* structure may be explained in terms of the W–O–W bond angles in the *xy*-plane. In the *P4-ncc* systems this angle is 174.60°, while in the *P4-nmm* system this angle is constrained by symmetry to 180°. The *P4-nmm* structure therefore has zero overlap with all antibonding O2p and the excess charge must be located on a W5d antibonding state. The difference in energy between bonding and antibonding W5d states is roughly 2 eV so that occupation of a spin-paired antibonding state can account for the ~4 eV by which the unrelaxed energy is anomalous.

**4. Orthorhombic *Pmnb*.** Upon relaxation, W–O bond splitting in the *x*-direction is 1.873–1.898 Å, in the *y*-direction it is 1.800–2.072 Å, and in the *z*-direction it is 1.791–2.169 Å. Compared to the undefected system this represents induced splitting in the *x*-direction, and decreased splitting in the *y*- and *z*-directions.

Four distinct sets of spin-coupled bands are apparent in the W6s levels and W6p bands are similar to the monoclinic systems. Level splitting of a group of bands that are degenerate between T–Y–S occurs between  $\Gamma$ –Z–T and X–U–R. As with the monoclinic systems there is a single spin-paired O2s band below the others. The O2s bandwidth increases to 2.10 eV, the O2p bandwidth increases to 7.10 eV ( $\Gamma$ – $\Gamma$ ), and the O2p–W5d gap decreases to 1.15 eV. Excess states are located at the  $\Gamma$ -point and have both W5d and O2p character.

5. *Triclinic P1*. W–O bond splitting upon relaxation is 1.819–1.946 Å in the *x*-direction, 1.788–2.063 Å in the *y*-direction, and 1.673–2.277 Å in the *z*-direction. There are substantial increases in splitting in both the *x*- and *z*-directions but a decrease in the splitting in the *y*-direction though the shortest bond in the *y*-direction remains unchanged.

The introduction of a vacancy induces spin-uncoupling and all bandwidths increase. The gap between O2p and W5d states decreases to 1.05 eV ( $\Gamma$ – $\Gamma$ ) for one spin component and 1.10 eV ( $Z$ – $Z$ ) for the other spin. The top O2p band is mainly composed of a  $p_z$  located on the oxygen furthest from the vacancy with other contributions from O2p.

The lowest energy spin component of the highest occupied band shows W–W dimer formation, bridging the gap across the oxygen vacancy. This level appears to consist of both W5d and O2p. The other spin component also comprises both W5d and O2p but there is no dimer formation. This is an important result since the only previous observation of a W–W long-range dimer bond was found in a theoretical study<sup>59</sup> of amorphous systems and this bond-type was conjectured as being of importance to electrochromism but a feature only of amorphous systems. The location of the excess states at the  $\Gamma$ -point is in agreement with the location of the lowest W5d states at this point in the undefected system.

6. *Summary of WO<sub>3</sub> Systems Containing an Oxygen Vacancy*. Structural relaxation around an oxygen vacancy yields an increase in the W–W distance across the vacancy in all cases and also induces changes to the degree of W–O splitting. The effect of this splitting can be understood in terms of bond overlap and bonding–antibonding interactions in the same way as in the undefected systems.

An added complication in the defected structures is the possible formation of a polaron. Excess electrons can therefore “dig their own hole” and the location of the lowest conduction band in the undefected system may not be the same as the occupied W5d levels in the defected system. Such a situation is exemplified by the *P21-c* system. The splitting–bandwidth relationship is unable to predict the large decrease in energy of the lowest W5d component at the A-point and a polaron is indicated. In all other systems excess electrons are located at the  $\Gamma$ -point as would be expected from the location of the lowest W5d states in the undefected systems.

Although the location of the lowest W5d band does not change for any system other than *P21-c*, the energy gap between the O2p and W5d states at this point does change. The energy gap is decreased from the undefected system value in all cases except the simple cubic and *P21-m* monoclinic systems. These are also the only two systems to show anything other than an increase in bandwidth, for all bandsets. In the simple cubic system a compression of the O2p bandwidth is noted and in the *P21-m* system a compression of the O2s bandwidth and unchanging W bandwidths are noted. Increased bonding–antibonding interactions in the simple cubic O2p and *P21-m* O2s bands are responsible for the increase in O2p–W5d gaps upon vacancy formation in these systems.

In the undefected systems, the charge states of the ions in WO<sub>3</sub> are all very similar, with the systems of greatest distortion all showing a slight reduction in the charge state of W ions. Simple cubic and tetragonal systems, which show no splitting in the *x*- or *y*-directions contain higher charge state W ions, this being indicative of less bonding/more antibonding. Upon the introduction of a vacancy, relaxation induces level splitting due to the inequivalence of ions present in the periodic cell. The charge states of the ions in each defected system are given

**TABLE 7: The Charge State of the Ions in a Pure Crystal and Adjacent to an Oxygen Defect for Several Crystal Phases and Vacancy Distributions<sup>a</sup>**

space group	<i>n</i> W	undefected WO <sub>3</sub>		WO <sub>3</sub> with an O vacancy		
		W <sup>x+</sup>	O <sup>y-</sup>	W <sub>1</sub> <sup>x+</sup>	W <sub>2</sub> <sup>x+</sup>	O <sup>y-</sup>
<i>Pm-3m</i>	8	5.78	1.93	5.36	5.52	1.83
<i>P21-c</i>	4	5.77	1.92	4.63	5.42	1.88
	8 <sup>b</sup>			5.18	5.38	1.87
	8 <sup>c</sup>			4.84	4.91	0.96
<i>P21-m</i>	4	5.77	1.92	4.83	5.18	1.78
<i>Pmnb</i>	8	5.77	1.92	5.00	5.14	1.90
<i>P4-nmm</i>	16	5.78	1.92	5.48	5.48	1.89
<i>P4-ncc</i>	16	5.79	1.93	5.47	5.47	1.81
<i>P1</i>	8	5.77	1.92	4.86	5.08	1.85

<sup>a</sup> *n*W is the number of W atoms in the unit cell. <sup>b</sup> Unit cell doubled in the *x*-direction. <sup>c</sup> Unit cell doubled in the *y*-direction.

in Table 7. Small polaron and IVCT models consider only integer charge states so the population analysis results are simplified in the following discussion. In the simple cubic and tetragonal systems the charge state of the W ions is approximately W<sup>5.5+</sup> for both ions adjacent to the vacancy. In orthorhombic and triclinic systems these ions correspond roughly to a pair of W<sup>5+</sup> ions while in the *P21-c* monoclinic system a roughly W<sup>4.5+</sup>/W<sup>5.5+</sup> pair is formed. The *P21-m* monoclinic system contains ions in a charge state intermediate to the orthorhombic and triclinic systems and the *P21-c* system. In the larger *P21-c* periodic cells a decrease in the splitting of ion charge states was noted. This effect may be attributed to decreased vacancy–vacancy interaction and the formation of a larger polaron.

The implication of the noted charge states is that W<sup>5+</sup> states are unlikely to form in simple cubic or tetragonal systems, though W<sup>5+</sup>/W<sup>6+</sup> pairs in the simple cubic structure would appear not unreasonable. Bipolaron W<sup>5+</sup>/W<sup>5+</sup> pairs may be possible in systems of intermediate W–O splitting, i.e., triclinic and orthorhombic systems, as well as the *P21-m* monoclinic system, while *P21-c* monoclinic WO<sub>3</sub> seems the only reasonable candidate for formation of W<sup>4+</sup>/W<sup>6+</sup> pairs. Increased vacancy–vacancy interaction would appear to promote the formation of such W<sup>4+</sup>/W<sup>6+</sup> pairs while decreased interaction favors W<sup>5+</sup>/W<sup>5+</sup> pairs. Population analysis of this sort should be treated with caution, however, and the collapse of ions into one charge state or another will most likely depend on the experimental probe used.

The low vacancy formation energy in the *P21-m* system and experimental observation of W<sub>4</sub>O<sub>11</sub> formation and clustering<sup>58</sup> indicate that a monoclinic phase is best able to incorporate oxygen deficiency and that W<sup>4+</sup>/W<sup>6+</sup> pairs may be stabilized in this way. A further piece of experimental evidence in support of this conjecture is that at room temperature single crystals with negligible defect populations tend to undergo a monoclinic–triclinic transformation.<sup>33</sup> It is worth remembering at this point that the phase described as *P21-m* within this work is strictly *P1* and our computational evolution of triclinic WO<sub>3</sub> from a monoclinic phase may mimic the experimental observation.

#### IV. Conclusions

The electronic structure of undefected phases is critically dependent upon the W–O bond length splitting in each direction. The shortest bond in the *y*-direction is the dominant parameter in determining band gap with a shorter bond causing increased bonding–antibonding interaction, this resulting in a larger band gap. Splitting in the *x*-direction has a similar though

lesser effect and splitting in the  $z$ -direction has the opposite effect. The first realistic GGA values and locations for the band gaps of these phases are reported herein.

The electronic structure of  $\text{WO}_{3-y}$  may be understood in the same way as the undefected phases. Relaxation around a vacancy causes changes in the shortest W–O bond in each direction. The effect of resultant bonding–antibonding interactions may be seen in all bandwidths and gaps. Two notable exceptions to universal bandwidth expansion and O2p–W5d gap decrease are in the  $P21-m$  and  $Pm-3m$  systems though the increase in O2p–W5d gap in these phases may be correlated with compression in the  $P21-m$  W6s and O2s, and  $Pm-3m$  O2p bands. The excess state in the  $P21-c$  system is located in a different position to the lowest unoccupied band in the undefected crystal, which when coupled with the observed populations indicates that a  $\text{W}^{4+}/\text{W}^{6+}$  polaron may form in strongly oxygen deficient  $\text{WO}_3$  or a  $\text{W}^{5+}/\text{W}^{6+}$  bipolaron may form in less oxygen deficient material.

**Acknowledgment.** We are grateful for support from an EU-INTERREG grant (Project 31514) and for allocations of time on the HPC(x) national facilities through the UKCP (GR/N02337/01) and Materials Chemistry (GR/N20607/01) consortia.

## References and Notes

- (1) Granqvist, C. G. *Handbook on Inorganic Electrochromic Materials*; Elsevier Science: Amsterdam, The Netherlands, 1995.
- (2) Granqvist, C. G. *Appl. Phys. A: Solid Surf.* **1993**, *57*, 3.
- (3) Deb, S. K. *Philos. Mag.* **1973**, *27*, 810–822.
- (4) Avellaneda, C. O.; Bulhoes, L. O. S. *Solid State Ionics* **2003**, *165*, 117–121.
- (5) Gavriluk, A. I. *Electrochim. Acta* **1999**, *44*, 3027.
- (6) Zhang, J.-G.; Benson, D. K.; Tracy, C. E.; Deb, S. K.; Czanderna, A. W. *J. Electrochem. Soc.* **1997**, *144*, 2022–2026.
- (7) Kubo, T.; Nishikitani, Y. *J. Electrochem. Soc.* **1998**, *145*, 1729.
- (8) Rougier, A.; Portemer, F.; Quede, A.; Marssi, M. E. *Appl. Surf. Sci.* **1999**, *153*, 1–9.
- (9) Washizu, E.; Yamamoto, A.; Abe, Y.; Kawamura, M.; Sasaki, K. *Solid State Ionics* **2003**, *165*, 175–180.
- (10) Jones, F. H.; Rawlings, K.; Foord, J. S.; Cox, P. A.; Edgell, R. G.; Pethica, J. B.; Wanklyn, B. M. R. *Phys. Rev. B* **1995**, *52*, R14392.
- (11) Kuzmin, A.; Purans, J.; Cazzanelli, E.; Vinegoni, C.; Mariotto, G. *J. Appl. Phys.* **1998**, *84*, 5515–5524.
- (12) Papaefthimiou, S.; Leftheriotis, G.; Yianoulis, P. *Solid State Ionics* **2001**, *139*, 135–144.
- (13) Badilescu, S.; Ashrit, P. V. *Solid State Ionics* **2003**, *158*, 187–197.
- (14) Faughnan, B. W.; Crandall, R. S.; Heyman, P. M. *RCA Rev.* **1975**, *36*, 177.
- (15) Schirmer, O. F.; Wittwer, V.; Baur, G.; Brandt, G. *J. Electrochem. Soc.* **1977**, *124*, 749.
- (16) Sun, S. S.; Holloway, P. H. *J. Vac. Sci. Technol.* **1984**, *A2*, 336.
- (17) Lee, S.-H.; Cheong, H. M.; Zhang, J.-G.; Mascarenhas, A.; Benson, D. K.; Deb, S. K. *Appl. Phys. Lett.* **1999**, *74*, 242.
- (18) Lee, S.-H.; Cheong, H. M.; Tracy, C. E.; Mascarenhas, A.; Czanderna, A. W.; Deb, S. K. *Appl. Phys. Lett.* **1999**, *75*, 1541.
- (19) Gerard, P.; Deneuille, A.; Courths, R. *Thin Solid Films* **1980**, *71*, 221.
- (20) Granqvist, C. G. *Sol. Energy Mater. Sol. Cells* **2000**, *60*, 201–262.
- (21) Bullett, D. W. *J. Phys. C: Solid State Phys.* **1983**, *16*, 2197–2207.
- (22) Goodenough, J. B. *Prog. Solid State Chem.* **1971**, *5*, 145.
- (23) Matthias, B. T.; Wood, E. A. *Phys. Rev.* **1951**, *84*, 1255.
- (24) Tanisaki, S. *J. Phys. Soc. Jpn.* **1960**, *15*, 566–573.
- (25) Salje, E. K. H. *Ferroelectrics* **1976**, *12*, 215.
- (26) Diehl, R.; Brandt, G.; Salje, E. *Acta Crystallogr.* **1978**, *B34*, 1105–1111.
- (27) Woodward, P. W.; Sleight, A. W.; Vogt, T. *J. Phys. Chem. Solids* **1995**, *56*, 1305.
- (28) Salje, E. K. H.; Rehmann, S.; Pobell, F.; Morris, D.; Knight, K. S.; Herrmannsdorfer, T.; Dove, M. T. *J. Phys.: Condens. Matter* **1997**, *9*, 6563.
- (29) Loopstra, B. O.; Boldrini, P. *Acta Crystallogr.* **1966**, *B21*, 158.
- (30) Loopstra, B. O.; Rietveld, H. M. *Acta Crystallogr.* **1969**, *B25*, 1420.
- (31) Ueda, R.; Ichinokawa, T. *Phys. Rev.* **195X**, 563–564.
- (32) Salje, B. *Acta Crystallogr.* **1975**, *B31*, 356.
- (33) Salje, E. *Acta Crystallogr.* **1977**, *B33*, 574–577.
- (34) Cazzanelli, E.; Vinegoni, C.; Mariotto, G.; Kuzmin, A.; Purans, J. *Solid State Ionics* **1999**, *123*, 67–74.
- (35) Kehl, W. L.; Hay, R. G.; Wahl, D. *J. Appl. Phys.* **1952**, *23*, 212–215.
- (36) Locherer, K. R.; Swainson, I. P.; Salje, E. K. H. *J. Phys.: Condens. Matter* **1999**, *11*, 4143–4156.
- (37) Brakken, H. Z. *Kristallogr.* **1931**, *78*, 484.
- (38) Ueda, R.; Kobayashi, J. *Phys. Rev.* **1953**, *91*, 1565.
- (39) de Wijs, G. A.; de Boer, P. K.; de Groot, R. A.; Kresse, G. *Phys. Rev. B* **1999**, *59*, 2684–2693.
- (40) Christensen, N. E.; Mackintosh, A. R. *Phys. Rev. B* **1987**, *35*, 8246.
- (41) Cora, F.; Patel, A.; Harrison, N. M.; Dovesi, R.; Catlow, C. R. A. *J. Am. Chem. Soc.* **1996**, *118*, 12174–12182.
- (42) Hjelm, A.; Granqvist, C. G.; Wills, J. M. *Phys. Rev. B* **1996**, *101*, 3945.
- (43) Stachiotti, M. G.; Cora, F.; Catlow, C. R. A.; Rodriguez, C. O. *Phys. Rev. B* **1997**, *55*, 7508.
- (44) Cora, F.; Stachiotti, M. G.; Catlow, C. R. A. *J. Phys. Chem. B* **1997**, *101*, 3945–3952.
- (45) Siedle, J. *Am. Chem. Soc.* **1989**, *111*, 1665.
- (46) Guery, J. *Solid State Electrochem.* **1997**, *1*, 199.
- (47) Yamaguchi, O.; Tomihisa, D.; Kawabata, H.; Shimizu, K. *J. Am. Ceram. Soc.* **1987**, *70*, C94–C96.
- (48) Balazsi, C.; Farkas-Jahnke, M.; Kotsis, O.; Petras, L.; Pfeifer, J. *Solid State Ionics* **2001**, *141–142*, 411–416.
- (49) Segall, M. D.; Lindan, P. J. D.; Probert, M. J.; Pickard, C. J.; Hasnip, P. J.; Clark, S. J.; Payne, M. C. *J. Phys.: Condens. Matter* **2002**, *14*, 2717–2744.
- (50) Vanderbilt, D. *Phys. Rev. B* **1990**, *41*, 7892.
- (51) Hammer, B.; Hansen, L. B.; Nørskov, J. K. *Phys. Rev. B* **1999**, *59*, 7413.
- (52) Perdew, J. P.; Zunger, A. *Phys. Rev. B* **1981**, *23*, 5048.
- (53) The Vanderbilt pseudopotential generator is available at: <http://www.physics.rutgers.edu/~dhv/uspp/#DOCUMENTATION>.
- (54) Gillan, M. J. *J. Phys.: Condens. Matter* **1989**, *1*, 689–711.
- (55) Azens, A.; Hjelm, A.; Bellac, D. L.; Granqvist, C. G.; Barczynska, J.; Pentjuss, E.; Gabrusenoks, J.; Wills, J. M. *Solid State Ionics* **1996**, *86–88*, 943–948.
- (56) Boulova, M.; Rosman, N.; Bouvier, P.; Lucazeau, G. *J. Phys.: Condens. Matter* **2002**, *14*, 5849–5863.
- (57) Koffyberg, F. P.; Dwight, K.; Wold, A. *Solid State Commun.* **1979**, *30*, 422.
- (58) Bonnet, J. P.; Onillon, M. *Solid State Ionics* **1984**, *12*, 337–342.
- (59) de Wijs, G. A.; de Groot, R. A. *Phys. Rev. B* **1999**, *60*, 16463.